Remote sensing of wave roller lengths in the laboratory

Merrick C. Haller[1] and P. A. Catalán[1,2]

[1] The optical intensity signals from surf zone waves in a laboratory flume are analyzed using several different phase-averaging techniques, and a methodology is developed for estimating wave roller lengths and local wave dissipation. The intensity signals (i.e., phase-averaged intensity profiles) of individual breaking waves are compared with the wave profiles measured by in situ wave gauges, and the optical signal of the wave roller is shown to ramp up from the toe of the wave roller on the front face of the wave to a maximum intensity at the wave crest. The remote sensing observations capture the growth, equilibrium, and decay phases of the roller as it propagates over a fixed bed arranged in a bar/trough morphology. Next, for the regular wave conditions considered here, the local maxima of the phase-averaged intensities are shown to better indicate the initial onset of wave breaking and the occurrence of wave breaking in the bar trough, as compared to the more commonly used time-averaged mean intensity. In addition, the phase-averaged profiles are used to measure the size of the roller, and these measurements are compared to previous observations of smaller-scale rollers in equilibrium. The observed roller lengths are shown to agree with predictions from a wave roller model and to provide a new physical link between the remotely sensed signal and roller dissipation. Finally, as an example application of these new data, a simple wave height inversion model is presented that allows an estimation of surf zone wave heights from the remotely sensed roller lengths.

1. Introduction

[2] Breaking waves at the ocean surface produce turbulence and entrain air bubbles, and the breaking process transfers a significant momentum flux into the water column [*Melville and Rapp*, 1985]. In fact, in the nearshore zone, the breaking process is the most important forcing mechanism for nearshore currents [*Svendsen*, 2006] and a contributor to the resuspension and transport of sediments. Since wave breaking is also highly variable in both space and time, the synoptic nature of most remote sensors makes them an effective tool for collecting wave breaking observations.

[3] Regular monitoring of wave breaking over large nearshore areas can be conducted using both optical (for a review see *Holman and Stanley* [2007]) and microwave radar [*Ruessink et al.*, 2002; *McNinch*, 2007; *Catalán et al.*, 2008] systems. One purpose of this type of monitoring is to observe the nearshore morphology or bathymetry on the basis of some approximate relationship between the local mean image intensity, wave breaking dissipation, and the

underwater topography. Our focus herein is on the first fundamental step of relating the image data to wave dissipation, which for optical data necessarily involves first separating the contribution of the active breaking region from the remnant foam.

[4] In the present work we first analyze the relationship between the optical intensity signal of individual breaking waves and the underlying waveshape in order to better understand the consequences of the averaging of image sequences, and in order to relate the intensity signal directly to dissipation in the wave roller using physical arguments. Specifically, the length of the wave roller is extracted from the intensity signal and is related directly to wave roller dissipation.

[5] The paper is organized as follows: in section 2 we review previous methods for analyzing the remote sensing signals of breaking waves, both for deep water whitecaps and for wave rollers in the surf zone. We also review the model for wave roller dissipation given by *Duncan* [1981] along with some relevant results from his laboratory observations. In section 3, the experimental data and basic processing procedures are described, including a new type of phase-averaging technique. In section 4, we compare the intensity waveform of breaking waves with the underlying waveform from synchronized in situ wave gauges. We also demonstrate the utility of phase averaging for determining the onset and cessation of wave breaking and describe the method for extracting the horizontal length scale of the wave

---

[1]Coastal and Ocean Engineering Program, School of Civil and Construction Engineering, Oregon State University, Corvallis, Oregon, USA.
[2]Now at Departamento de Obras Civiles, Universidad Técnica Federico Santa María, Valparaiso, Chile.

rollers as a function of cross-shore location. In section 5, we first demonstrate that our remotely measured roller lengths are consistent with the smaller-scale results of *Duncan* [1981]. Then we utilize a standard model for the wave roller energy balance to show that our observations agree with the model predictions and, thus, that the observed roller lengths can be related to wave roller dissipation for a given choice of roller angle. Finally, in section 6 we introduce and test a simple inverse model that estimates wave heights in the surf zone on the basis of roller length and bathymetry observations.

2. Some Previous Work

2.1. Intensity Signal From Breaking Waves

[6] The relationship between the optical intensity received by a camera and the underlying water surface elevation depends on the mechanism by which the waves are imaged. When waves are not breaking, the principal imaging mechanism is specular reflection of the incident light from the free surface. This specular reflection depends on the instantaneous angle defined by the light source, the water surface, and the camera, and also the relative angle between the direction of wave propagation and the camera [*Stilwell*, 1969]. In contrast, the bubbly water surface produced by wave breaking is generally treated as an isotropic (Lambertian) scattering surface for the visible band of light [*Gordon and Jacobs*, 1977; *Tratt et al.*, 2002].

[7] In oceanographic remote sensing operating in the visible band, signals from bubbles at the sea surface are referred to as whitecaps and can be classified into two stages: Stage A, which corresponds to the region of active breaking; and Stage B, which is the area of remnant foam left behind the propagating wave crest [*Bondur and Sharkov*, 1982; *Monahan and Woolf*, 1989]. We note that there are some differences between the breaking behaviors (and terminology) in the open sea versus the nearshore. In the open sea, a Stage A whitecap propagates with the wave crest but generally has a limited lifespan (∼4 s) and then transitions to Stage B (foam) and decays exponentially depending on wind input and nonlinear energy transfers [*Walker*, 1994].

[8] In the surf zone, the active breaking portion is referred to as the wave roller and, since breaking is induced by interaction with the sea bottom, once it is initiated it tends to persist for a significantly longer time. For example, on a monotonically sloping beach the wave roller would be expected to propagate with the wave crest from the breaker line to the point of complete wave decay at the shoreline, a distance on the order of a few wavelengths (or ∼12−20 s). However, on a beach where breaking is initiated over a bar, the wave roller will likely decay and may completely disappear as the wave propagates into the deeper trough region, but reappear at the shore break. Breakers in the surf zone also produce remnant foam; but, for both whitecaps and wave rollers it is generally agreed that the active breaking region is the area of primary dynamical interest.

[9] For wave breaking analysis, the first step in the image processing is the separation of whitecaps (or wave rollers) from the nonbubbly portions of the sea surface image. This is most often done with an intensity thresholding method, where all pixels with intensities above a threshold value are attributed to areas of wave breaking. The threshold can be chosen with varying levels of subjectivity and is sometimes allowed to vary between images in a sequence [e.g., *Ross and Cardone*, 1974; *Kraan et al.*, 1996; *Stramska and Petelski*, 2003; *Lafon et al.*, 2004; *Sugihara et al.*, 2007; *Callaghan et al.*, 2008]. Though not described this way, these threshold methods are essentially based on the cumulative pdf of the recorded pixel intensities. The percentage of image pixels above the threshold (i.e., whitecap area) is determined for a range of thresholds and where the percentage shows the least dependence on threshold, i.e., where the cumulative pdf has the smallest slope [see *Sugihara et al.*, 2007, Figure 5], is where the threshold is usually set.

[10] With regard to whitecap observations in the visible band, one thing to be noted is that distinguishing the active breaking regions from the remnant foam is a challenge and is infrequently attempted. On the other hand, other results suggest that sensors operating outside the visible band may better distinguish active breaking from foam; examples using infrared sensing of whitecaps were given by *Jessup et al.* [1997] and *Marmorino and Smith* [2005]. In the surf zone, *Haller and Lyzenga* [2003] showed an increased contrast between active breaking and foam using an X band microwave sensor. However, for optical sensors, most often it is the total whitecap coverage that is determined; although, *Ross and Cardone* [1974] and *Monahan and Woolf* [1989] used a subjective separation method based on relative intensities and *Kerman and Dernier* [1994] give a separation method based on a multifractal representation of the image intensities.

[11] A second aspect to note regarding optical sensing of whitecaps is that, once a threshold is chosen, the images are converted to binary maps corresponding to either whitecaps or unbroken water; hence, the observed relative intensity values are reduced to ones and zeros and the intensity magnitudes are no longer used in the analysis. Instead, it is the measure of the spatial extent of wave breaking that is used. However, in the surf zone some other approaches to image analysis have been taken.

[12] Historically, the primary image product used to estimate surf zone dissipation has been the "time exposure," which is the average of a sequence of images or of a pixel time series [*Lippmann and Holman*, 1989; *van Enckevort and Ruessink*, 2001]. Typically it is the local magnitude of the time-averaged mean intensity that is of interest. An alternative, and more direct, remote sensing approach was given by *McGregor et al.* [1998] who related the observed surface orbital velocities from Doppler radar data to the wave energy flux (and dissipation) in the surf zone. Unfortunately, measurements of orbital velocities are not available from most optical systems.

[13] Recently, *Aarninkhof and Ruessink* [2004] gave an updated method for extracting the wave breaking contribution from that of remnant foam in optical time exposures and compared the cross-shore profile of mean intensity to several modeled dissipation proxies. This work is now being applied in increasingly sophisticated data assimilation systems for bathymetric estimation [*Aarninkhof et al.*, 2005; *van Dongeren et al.*, 2008]. However, one issue with these previous efforts is that the intensity signal has not been related to dissipation using direct physical arguments. In fact, the optical systems used for coastal monitoring are not

radiometrically calibrated (a nontrivial task); hence, the overall magnitude of the mean intensities are essentially arbitrary, but assumed to be proportional to a local proxy for dissipation. Yet as is illustrated in the present work, the mean intensities represent an average over various, complexly correlated contributions of foam, differences in the frequency of breaking, and variations in wave roller size. In addition, there is the potential for a nonconstant maximum optical intensity for different breakers (even if an individual breaker is a Lambertian scatterer), which will have a nonlinear effect on the mean intensity even if a relationship between intensity magnitude and dissipation were determined.

[14] In addition, the empirical relationship between the mean intensity signal and dissipation given by *Aarninkhof and Ruessink* [2004] was specifically developed for barred morphologies with the expressed purpose of locating the bar crest (the location of the cross-shore maximum of the mean intensity is a key matching variable). Therefore, the methodology does not appear to be applicable to nonbarred beaches, and especially not to extracting the wave dissipation on the time scales of individual waves or wave groups, the latter being important in the driving of low-frequency surf zone motions. Finally, the methodology of *Aarninkhof and Ruessink* [2004] is constructed upon an ad hoc model for the intensity signal of individual breaking waves that, while proven useful in the broader goal of tracking sandbar position, is found to be in error in some details when the image intensities of individual breaking waves are directly compared to the underlying surface signal (see section 4.1). Nonetheless, it is acknowledged that their methodology was successful at adapting a simple model for individual breaking intensities to the difficult real-world problem of dissipation of a random wavefield on a field beach.

2.2. Model for Wave Roller Dissipation

[15] The earliest description of the wave roller and wave roller dissipation was given by *Duncan* [1981]. This approach is now commonly used and in it the roller dissipation, D, is considered to arise from the shear stress exerted by the wave roller on the sloping front face of the underlying wave. This shear stress must balance the weight of the wave roller. The projection of this shear stress, τ_s, into the wave propagation direction leads to the following expression for the wave-averaged rate of energy dissipation per unit planform area:

$$D = \frac{C\tau_s \cos\theta}{L} = \frac{\rho g A}{T} \sin\theta\cos\theta, \tag{1}$$

where ρ is the mass density of the roller (usually taken as the same as water), C is the translation speed of the roller and taken as equal to the wave phase speed, T is the wave period, A is the area of the roller in vertical cross section, and θ is the mean surface slope under the roller. Hence, there is a straightforward relationship between A and roller dissipation; but, the cross-sectional area A is a difficult measurement to obtain, except in some laboratory situations [e.g., *Govender et al.*, 2002].

[16] The work of *Duncan* [1981] also contains measurements of A, the roller along-slope length (here denoted L_r'), and θ from deep water breaking waves in equilibrium.

While *Svendsen* [1984] used the parameterization $A/H^2 = 0.9$ (determined from Duncan's measurements) in one of the earliest models for wave rollers in the surf zone, we note that the L_r' measurements have not yet been exploited. Here we will assume that the roller geometry is self-similar through most of its life cycle; hence, A and L_r' are simply related. This is supported by Duncan's conclusion that the ratio of the breaking region thickness (A/L_r') to length is constant for all observed conditions. From his equilibrium data he obtained:

$$\frac{A}{L_r'^2} = 0.11 \pm 0.01. \tag{2}$$

For comparison, this relationship shows much less variation than $A/H^2 = 0.9$ (± 0.25). This suggests that measurements of the roller length can be related to area and then related to dissipation.

3. Experimental Data

[17] In order to examine in detail the optical intensity signal from individual breaking waves and to test whether remotely sensed roller lengths can be used to make direct estimates of wave dissipation, we further analyze the laboratory data of *Catalán and Haller* [2008]. These data consist of video observations of regular breaking waves over a fixed bed. The synchronous in situ wave measurements allowed us to compare the intensity signal with the underlying waveshape. In addition, using the laboratory provided additional control and simplifications, such as being able to adjust the degree of wave breaking through the surf zone and reducing the persistent foam because of the lack of dissolved biological material. We recognize that the artificial lighting in the laboratory can certainly complicate the optical signals. However, this mostly affects the signals from nonbreaking waves in the shoaling zone, which we do not analyze herein.

3.1. Setup

[18] The experimental data were collected in the Large Wave Flume (LWF) at the O.H. Hinsdale Wave Research Laboratory (Oregon State University). The LWF coordinate system has the x axis pointing onshore along the centerline with the origin at the wave maker. The bathymetry was configured in a piecewise continuous, barred morphology (concrete slabs, no sediment). The water depth at the wave maker was 4.27 m. Six resistance-type wave gauges were used to measure free surface elevation and were sampled at 50 Hz. The wave gauges were installed at cross-shore locations $x = 23.45, 45.40, 52.73, 60.04, 70.99$ and 81.97 m as shown in Figure 1. The six experimental regular wave conditions are listed in Table 1. Measured wave heights for three of the experimental runs are shown in Figure 1, as well as the bathymetry. The wave heights for the other tests are shown in Figures 12 and 13. The breaking wave height values given in Table 1 correspond to the largest measured mean wave height for a given condition and may underestimate slightly the wave height at the break point. The Iribarren numbers near the break point, $\xi_b = \beta/\sqrt{H_b/L_o}$, given in Table 1 were computed with a representative slope $\beta = 1/24$, corresponding to the shoreward face of the bar,
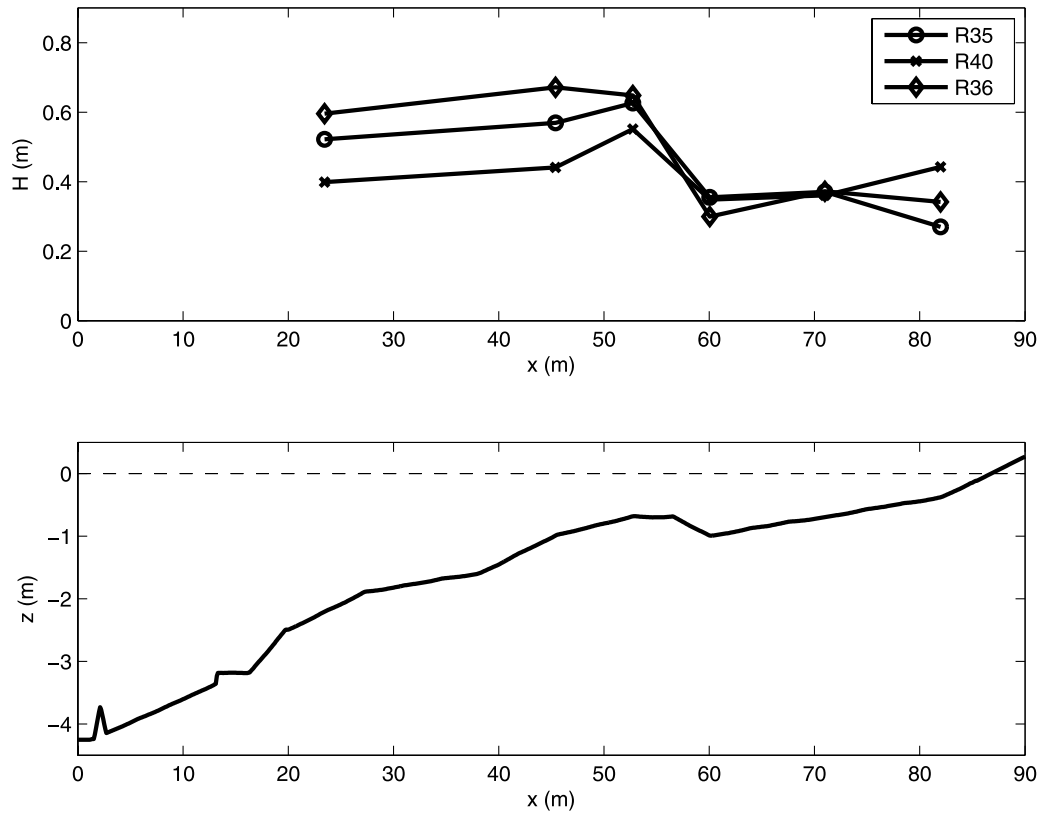
Figure 1. Experimental conditions: (top) measured wave heights for R35 (circle), R40 (cross), and R36 (diamond) and (bottom) vertical elevation of the fixed bed.

which is where waves began to break for most of the conditions. Further details of the experimental procedure can be found in the work by *Catalán and Haller* [2008].

[19] Simultaneous video observations were collected using an ARGUS III video station [*Holman and Stanley*, 2007]. At the time of the experiments the station consisted of three digital cameras mounted near the laboratory ceiling and aimed at different sections of the flume. The cameras were 9.88 m above the still water level and the field of view of the cameras spanned the cross shore from $x = 41.7$ m to the dry beach. All cameras were sampled at 10 Hz and the method for synchronizing the cameras with the wave gauges is given in Appendix A.

[20] Once time synchronization between the wave gauges and camera systems was achieved, we utilized a cross-shore pixel array along the longshore coordinate $y = 1.2$ m for the analysis of the intensity data. Registration of the pixels to the lab coordinate system involved mapping the data to the elevation of the still water level and interpolation to a uniform cross-shore grid resulting in a total of 5736 pixels along the array with a resolution of $\Delta x = 1$ cm. For times and locations where the water surface deviates significantly from the still water level, such as at the wave crests, there is a misregistration error that represents a perspective shift between the location of the crest and the location it is mapped to in the pixel array. The correction for this error is also described in Appendix A. In addition, in order to account for differences in exposure settings between cameras, the pixel intensity time series were adjusted by a constant factor to provide continuous mean intensity values

across camera boundaries in the pixel array. More details of this procedure can be found in the work by *Catalán* [2005].

3.2. Data Processing

[21] In the initial processing of the optical intensity data, the time series from the cross-shore pixel array were arranged into a time-space map of pixel intensity, or "time stack." After removing the startup portions of all sensor records, the final record lengths for the different experimental runs included between 48 and 126 waves (see Table 1). In order to remove the slight variations (± 0.001 s) in the camera sampling rate, these truncated time stacks were then resampled to a uniform 10 Hz grid.

[22] The raw camera resolution varies from 1 cm^2/pixel close to the cameras ($x = 52.7$ m) to 8 cm^2/pixel near the shoreline ($x = 86.8$ m). However, the original rectified and interpolated pixel array was generated with a resolution of 1 cm in order to preserve the raw camera resolutions. As a last

Table 1. Wave Conditions[a]

Run	T (s)	Number of Waves	H_o (m)	$\frac{H_o}{L_o}$	H_b (m)	ξ_b
35	2.7	126	0.57	0.050	0.63	0.18
40	4.0	81	0.40	0.016	0.55	0.28
36	4.0	97	0.63	0.025	0.67	0.25
37	5.0	77	0.51	0.013	0.78	0.29
38	6.0	61	0.47	0.008	0.68	0.38
33	8.0	48	0.37	0.004	0.73	0.49

[a]T, wave period; number of waves in data record; H_o, deep water wave height; H_o/L_o, deep water steepness; H_b, breaking wave height; and ξ_b, Iribarren number at the break point.
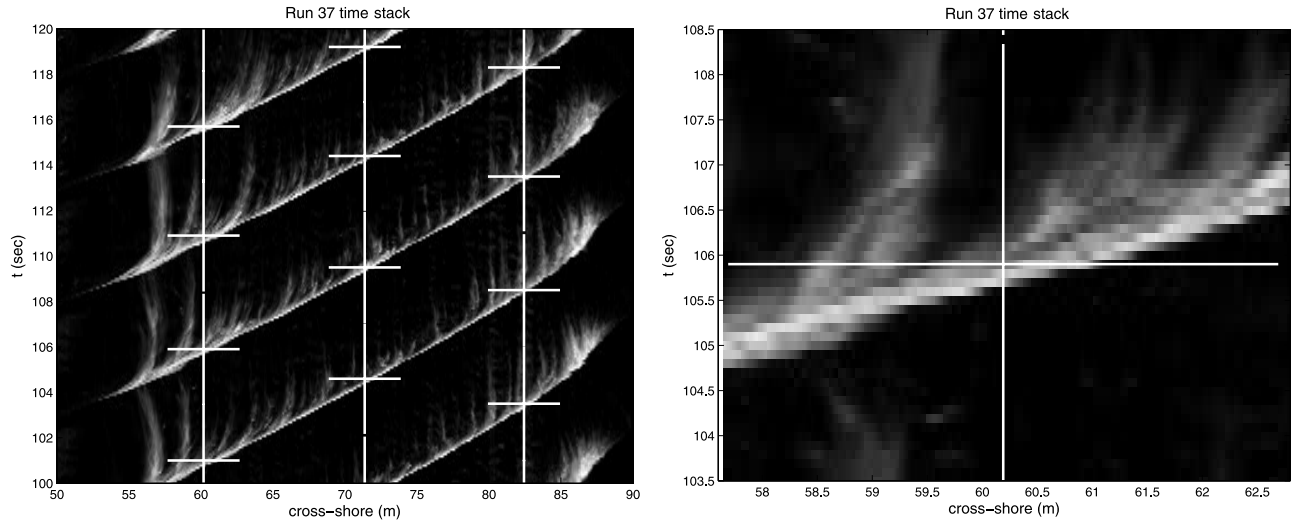
Figure 2. (left) Example time stack: vertical lines represent the time partitions (5 s for this run) used for phase averaging (partitions occasionally overlap), and horizontal lines represent 5 m spatial partitions centered on the wave gauge locations (three shoreward gauges shown here). (right) Single breaking event from time stack in Figure 2 (left).

step, the time stacks were spatially filtered with a 10-point (10 cm), zero-phase, forward and reverse digital filter in order to better reflect the overall resolution of the array and to reduce noise. An example portion of a processed time stack is shown in Figure 2.

[23] For the comparison of the intensity waveforms with the underlying breaking waves, the first step was to identify the passage of wave crests at five of the in situ wave gauges (no breaking occurs at the offshore gauge). Although the wave conditions were regular, there were small oscillations of the observed wave periods because of long-period standing waves in the flume as shown by *Haller and Özkan Haller* [2007]. Those previous results showed that the standing wave (seiching) amplitudes ranged from around 0.5 cm at the break point to $1-2$ cm near the shoreline and the main observed effect was a regular oscillation in the incident wave period. A regular modulation in the wave height at the breaker line of approximately 1.5 cm was also predicted (by an analytic model), but not observed in the data. However, the time stack data do indicate long-period modulations in the initiation of breaking, but the nature of how the standing waves influence the initiation of breaking is a subject of further work. For the present work, the wave gauge records were first high-pass filtered at 0.1 Hz to remove the low-frequency signal of the standing wave modes of the flume (<4% of total variance). Next, a zero-upcrossing method was used to demarcate individual waves, identify the wave crest times ($t_{g,i}$, where $i = 1$ to N, N is the total number of waves), and also calculate the mean wave height for each wave gauge and all experimental runs.

3.3. Phase-Averaging Methodologies

[24] For processes that occur at the wave time scale, the method of phase averaging in time is an effective way to remove shorter time scale variations due to turbulence and small-scale processes. In most analyses the phase averaging is performed in the time (or frequency) domain using a single-point time series of water surface elevation or veloc-

ity, and narrow-banded wave conditions are required. For the present analysis we performed two different types of phase averaging, one in time and one in space.

[25] For the phase averaging in time, we partition each wave gauge time series, $\eta(x_g, t)$ where x_g is the gauge location, into sections of equal duration corresponding to the intervals $(t_{g,i} - T/2) \leq t_{g,i} \leq (t_{g,i} + T/2)$. These are then arranged into a matrix ensemble with the wave crests as the center values. Either the average or the median value over the number of waves in the ensemble then gives the phase-averaged signal, $\langle \eta(x_g, t) \rangle$ (where $-T/2 \leq t \leq T/2$), which represents a smoothed version of a single wave. Here, for all signals from both sensors we have used the median values because they are less sensitive to outliers.

[26] The intensity time stacks are partitioned in the same fashion using the crest times from the wave gauge analysis. The corresponding phase-averaged intensity signal is then given by $\langle I(x'_g, t) \rangle$ where x'_g is the spatial location of the wave crest in the pixel array after correction for misregistration. In other words, x'_g is where the crest appears in the pixel array because of the misregistration effect (see Appendix A). In order to simplify the comparisons between the two signals, the intensity time series were linearly interpolated to the 50 Hz grid of the wave gauges before phase averaging.

[27] Since the time stacks are highly resolved space-time data, we also perform a new type of phase averaging in space in order to analyze the spatial variation of the wave breaking intensity signal. For the spatial phase average, the time stacks are partitioned into individual sections I over the regions $[(x'_g - 2.5) < x'_g < (x'_g + 2.5), t_{g,i}]$, which represent 5 m spatial intervals centered on individual wave crest times at each gauge. Again these are arranged into a matrix ensemble and the median over the number of waves gives the spatial phase-averaged signal $\langle I(x) \rangle$ for each wave gauge and each experimental run.

[28] Some examples of the partitions used in the space and time phase averaging are shown as white lines on the

time stacks in Figure 2. The vertical lines show partitions in time for the three shoreward wave gauges (partitions occasionally overlap). The horizontal lines show 5 m spatial partitions and are centered on the wave gauge locations. The intersections of the horizontal and vertical lines represent the space-time locations of individual wave crests $(x'_g, t_{g,i})$ and a closeup view of a single breaking event is shown in Figure 2 (right). From Figure 2 it is interesting to note the episodic nature of the remnant foam that is generated as the wave rollers progress in space and time. At almost regular intervals, foam is released from the wave crest and propagates only slowly, if at all. These events appear as regular filaments spreading upward from the bright roller trajectories. In general, the optical signal from these foam filaments decays to the background (nonbreaking) levels in less than a wave period for all the experimental cases. However, as can be seen from Figure 2 (right), the relative location of the wave gauges with respect to these foam release events can affect the net contribution of foam to the individual time or space series.

4. Results

4.1. Phase-Averaged Roller Signal: Time Variation

[29] The optical signals phase averaged in time are shown in Figure 3 as well as the signals from three individual breaking wave events in order to illustrate the effect of the phase-averaging process. Each plot in Figure 3 shows several individual wave and intensity records superimposed on the phase-averaged signals, $\langle \eta(x_g, t) \rangle$ and $\langle I(x'_g, t) \rangle$. Only the signals from gauges 2 to 5 are shown because the waves did not break at gauge 1 for any of the wave conditions.

[30] It is clear from Figure 3 that the intensity signal generally has more wave-by-wave variability than the surface elevation signal. This happens for two reasons. One is that the production of remnant foam is variable in both space and time as shown in Figure 2, which contributes to the variability of the intensity signal. The second is that, at certain locations in the bar trough, for certain runs waves only broke intermittently (e.g., 19% run 36 gauge 4, 29% run 36 gauge 5). This led to large wave-by-wave variations in the intensity signal because, while the surface elevation signal is not very different for breaking versus nonbreaking waves, the imaging mechanism and resulting intensity signal is very much different.

[31] By reviewing handheld camcorder records (not from the ARGUS station) of the experimental conditions, we determined that the intensity signals at the different gauge locations derive from the transition from plunging breaker (gauge 2) to established wave breaking roller (gauge 3) to decaying roller (gauge 4) to initiation of the shore break (spilling breaker, gauge 5). Correspondingly, the intensity signal shows the initiation of an isolated bright region at gauge 2. At gauge 3, the intensity signal of the well established roller has a steep front face and decaying tail. The decaying tail represents the signal from remnant foam and injected bubbles rising to the water surface and is generally nonpropagating (see Figure 2).

[32] Figure 3 also illustrates the differences between the intensity signals from breaking versus nonbreaking waves. For example, at gauges 4 and 5 only 19% and 29% of the waves were breaking, respectively (percent breaking values

are shown in Table 2). However, the phase-averaged signals in Figure 3 were determined from the ensemble of all waves both breaking and nonbreaking. At gauges 4 and 5 the phase-averaged intensities are much reduced as compared to gauges 2 and 3. The few individual intensity events shown for gauge 5 happen to represent breaking events, but it is evident that the inclusion of the 71% nonbreaking events severely dampens the phase-averaged signal. This also gives some sense as to how the averaging process affects the intensity signals in the even more heavily averaged time exposure product.

[33] It is also possible to see evidence of pixel saturation in the signal for gauge 3, this is indicated by the flat tops of a few of the individual intensity signals. In general, the intensity values from a given camera vary from 0 to 255 but after processing the saturated values (255) can be shifted lower because of the image merging and filtering processes. In order to quantify the amount of data affected by image saturation, the percentages of saturated points, defined as intensity values within 5 of the maximum for a given camera, were tabulated and are also given in Table 2. By counting all values within 5 of the maximum we allow for the effects of filtering and interpolating and make a likely conservative (over) estimate of the percentage saturation. The percentage of saturated data points is generally ≤5%.

[34] It is of interest to more directly relate the phase-averaged signals from each sensor. Figures 4 and 5 show an overlay of the time phase-averaged water surface and intensity signals from gauges 2 to 5 for most of the experimental runs (the ones with the highest breaking occurrence for all gauges). Figures 4 and 5 show that for breaking waves the peak intensity occurs very near the wave crest. The intensity ramps up very quickly on the front face of the wave where the roller is located and then tails off over the remnant foam on the trailing portion of the wave. The small time differences between the peaks in each signal, normalized by wave period, are given in Figures 4 and 5 as well (negative values indicate the intensity peak leads the wave crest). Considering the 10 Hz sampling rate of the cameras, the resolution of the calculated time differentials is $\Delta t/T = 0.01 - 0.03$. Hence, since the normalized time differences between the different signal peaks are always ≤0.04 (the outlier value for R36 g5 is due to low percent breaking), it is clear that the intensity peaks coincide with the wave crests within the resolution of the measurements.

[35] The observation that the intensity peaks coincide with the wave crests contrasts with the roller intensity model of *Aarninkhof and Ruessink* [2004] where the roller intensity is assumed to have a step function increase in intensity at the roller followed by an exponential time decay lasting for one-half the wave period. That model implies that the brightest signal comes from the leading edge of the roller. While it is possible that the artificial lighting in the laboratory might influence the location of the maximum intensity relative to the wave crest, we note that the field data of *Lippmann and Holman* [1991, Figure 1] appear to qualitatively confirm our result as well.

[36] For runs where significant breaking occurred at gauge 2 (runs 36, 38, and 33) the intensity peak leads the wave crest slightly ($\Delta t/T \approx -0.03$). For these cases the plunge point was very near gauge 2; hence, the brightest signal is coming from the splash up of the plunging jet,
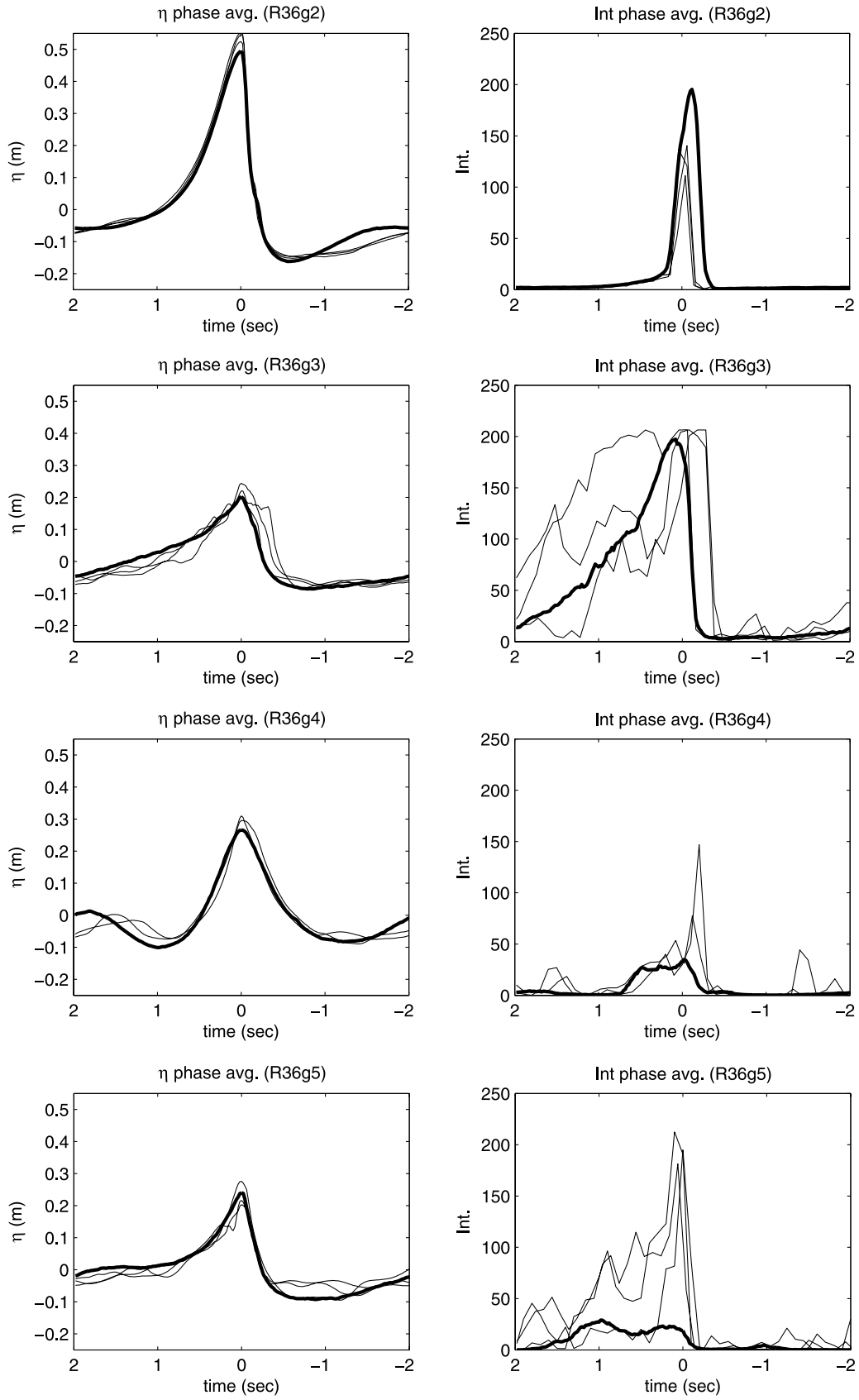
Figure 3. (left) Water surface elevations and (right) intensity signals from three individual waves (run 36) are shown as thin lines. Signals phase averaged in time are shown as thick lines. Gauge location is indicated by gauge number above each plot.

Table 2. Percent Breaking and Percent Saturations From Intensity Signals at All Gauge Locations x_g' and Experimental Runs

	Gauge 2		Gauge 3		Gauge 4		Gauge 5	
Run	Percent Breaking	Percent Saturation	Percent Breaking	Percent Saturation	Percent Breaking	Percent Saturation	Percent Breaking	Percent Saturation
35	1	0	100	4	29	0	100	0
40	0	2	100	4	36	0	83	1
36	100	0	100	5	19	0	29	0
37	10	0	100	0	100	0	100	0
38	100	0	100	0	100	0	100	0
33	96	0	100	6	100	0	100	2

which naturally leads the wave crest. The data do not indicate that the splash up is often separated from the plunger by a dark area. The wave roller becomes fully established shoreward of the plunge point.

4.2. Comparison Between Mean and Phase-Averaged Signals

[37] With the goal of better understanding the relationship between wave dissipation and the different image products, we will compare the cross-shore variation of the intensity mean (time exposure) with the underlying signal of an individual (phase-averaged) breaking wave. The time exposure represents the average along the vertical axis of the time stack shown in Figure 2. This averaging process clearly will smear together the signal from the wave rollers and that of the remnant foam (and the nonbreaking portions of the signal), and the degree to which foam influences the time exposure is not well understood.

[38] Since, for this comparison we need the phase-averaged signal at all cross-shore locations, we do not have the luxury of demarcating the individual waves using the crest times recorded by the wave gauges. Instead we simply divide the time stack along the time axis into equal sections one wave period in duration and take the median value over all waves at a given space and relative time location. Hence, there is some smearing of the signal because of wave period modulations and locally intermittent breaking. This phase-averaged time stack gives a picture of the evolution of an individual wave, $\langle I(x, t) \rangle$, across the entire domain as shown in Figure 6 (top).

[39] Next, we track the maximum intensity, $I_{max}(x)$, taken along vertical transects in the phase-averaged time stack. As we have seen in section 4.1, these intensity maxima are located at the wave crest. So $I_{max}(x)$ represents the intensity of the roller as it propagates through the surf zone, and it is not contaminated by the presence of foam or by averaging with other nonbreaking portions of the record. In Figure 6 (bottom) the $I_{max}(x)$ signal is compared with the standard time exposure signal, $I_{mean}(x)$, for one run. Figure 6 demonstrates that the cross-shore profile of the crest intensity provides a very precise determination of the onset of breaking where there is a sharp increase in $I_{max}(x = 52$ m). In contrast, the smearing effect of the time exposure process provides a much less sharp indication of the onset of breaking and a significantly decreased dynamic range across the profile. The maximum of I_{mean} is shifted shoreward relative to the cross-shore maximum of I_{max}. This is a direct result of cross-shore variations in the length of the decaying intensity tails for individual waves (i.e., the tails

get longer away from the break point) and in the variation of the location where remnant foam is produced.

[40] In addition, the decreased dynamic range of the time exposure signal makes it more difficult to determine the breaking conditions in the trough. As indicated in Figures 4 and 5, wave breaking did not cease in the trough of the bar for runs 37, 38, and 33. The variation of the new I_{max} parameter for these runs shown in Figure 7 also reflects this, as the crest intensity steadily decays through the trough but is still larger than the offshore (nonbreaking) values. On the other hand, it is very difficult to detect the occurrence of wave breaking in the trough by looking at the I_{mean} signals from these runs. While a quantitative relationship between I_{max} and wave dissipation is not attempted here, Figures 6 and 7 suggest that I_{max} gives a much clearer indication of the onset of wave breaking and the spatial extent of the surf zone. However, it is recognized that the phase-averaging technique requires very narrow-banded wave conditions, not often found in the field. Extracting the I_{max} parameter would require a more complex tracking mechanism to identify individual breakers in field data.

4.3. Phase-Averaged Roller Signal: Spatial Variation

[41] The spatial variation of the phase-averaged signals are useful because they provide an instantaneous snapshot of the intensity signal of an individual breaking wave. The full image snapshots often used in whitecapping analyses essentially consist of a number of these individual signals having a range of wavelengths. Unfortunately, counterpart water surface snapshots cannot be obtained by the few in situ wave gauges used in these experiments.

[42] The spatial variation of the individual wave rollers are shown relative to the respective wave gauge locations in Figure 8. For the spatial phase averaging we have limited the ensembles to only breaking waves, as defined by the occurrence of at least two points in space with intensities above a threshold value (defined in section 5.1). Hence, for gauge 2 runs 35 and 40 there is no spatially phase-averaged signal (waves were not breaking there). If we consider the intensity signal as a locally permanent waveform, then we would expect the spatial phase-averaged signals in Figure 8 to match the temporal phase-averaged signals of Figures 4 and 5. Here Figures 4, 5, and 8 indicate that while the time and space signals are similar there are some differences, mostly in the structure of the trailing edge.

[43] Figure 8 (top three plots) shows runs where breaking had almost ceased in the trough shoreward of the bar (gauge 4, runs 35, 40, and 36). The dominant feature of these profiles is the strong decrease in intensity for the waves in the trough. This suggests that the intensity magnitude of an
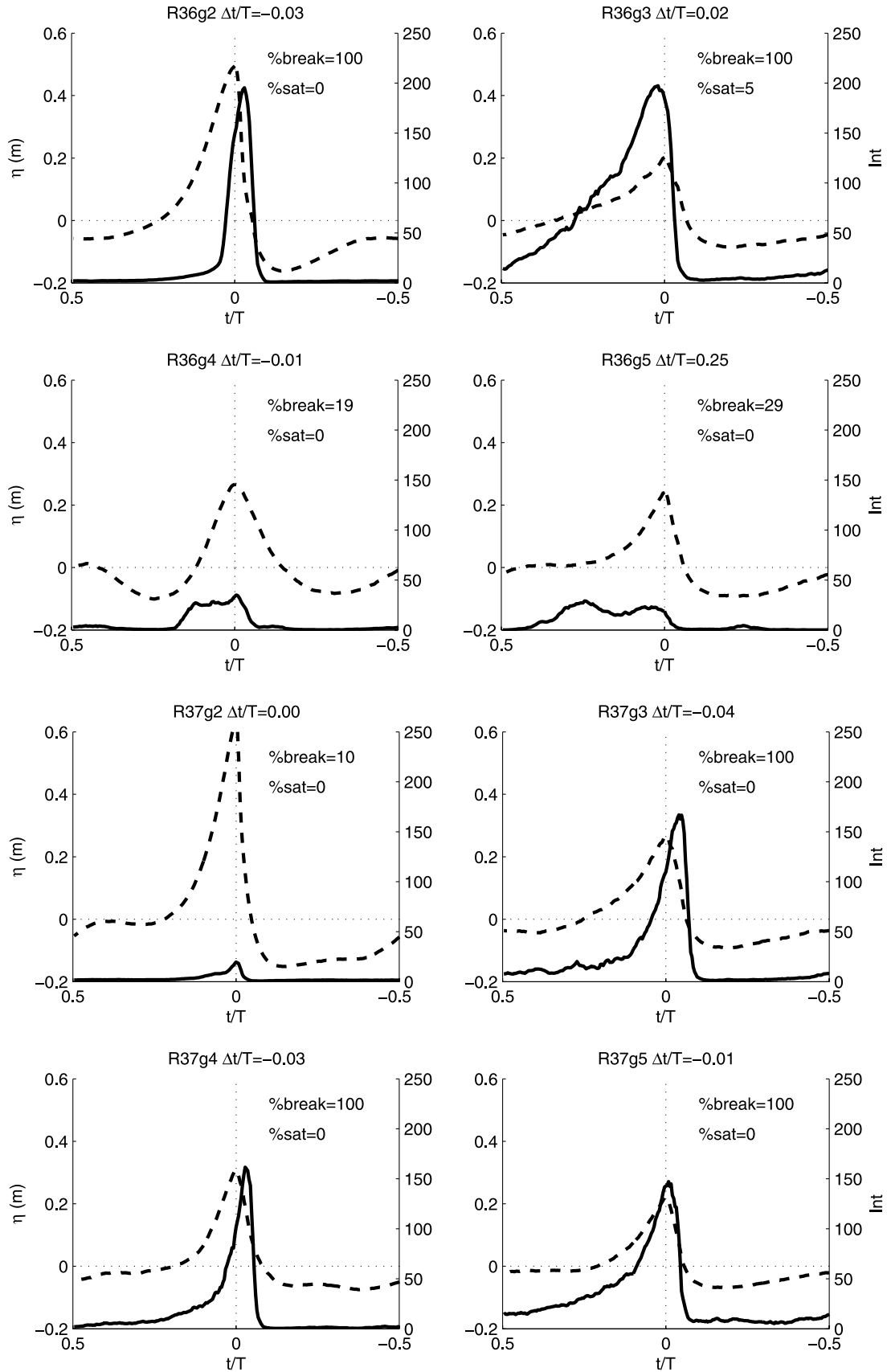
Figure 4. Surface elevations phase averaged in time (dashed lines) and optical intensities (solid lines) from gauges 2 to 5 and runs 36 and 37.
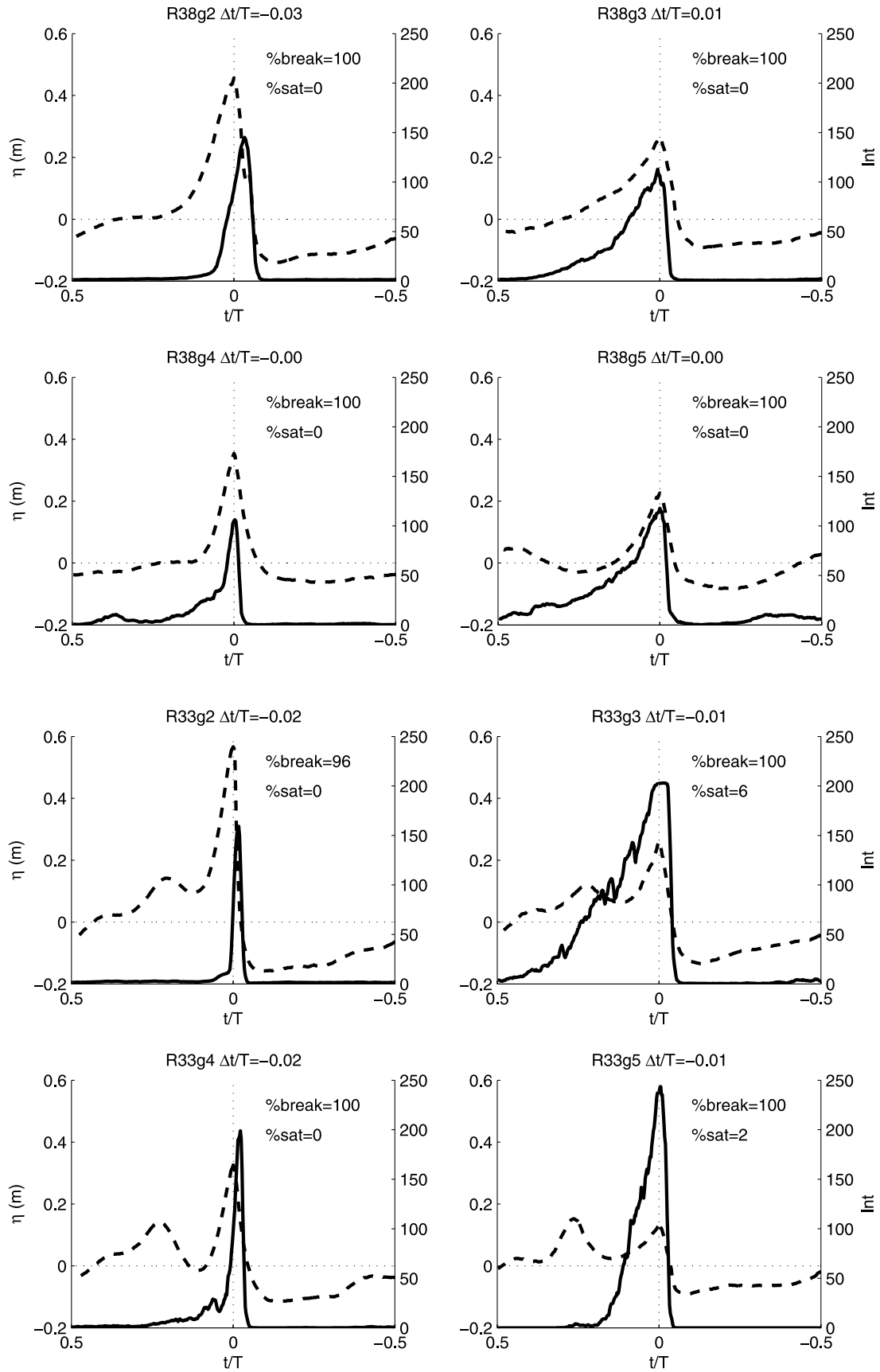
Figure 5. Surface elevations phase averaged in time (dashed lines) and optical intensities (solid lines) from gauges 2 to 5 and runs 38 and 33.
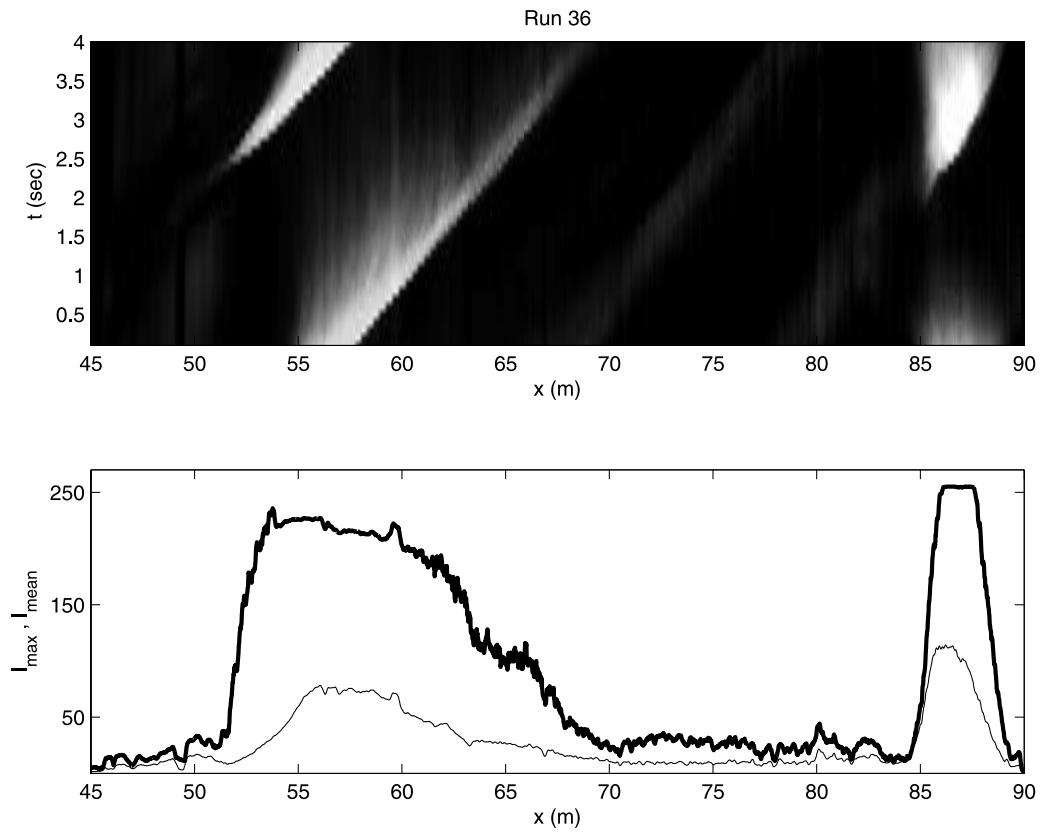
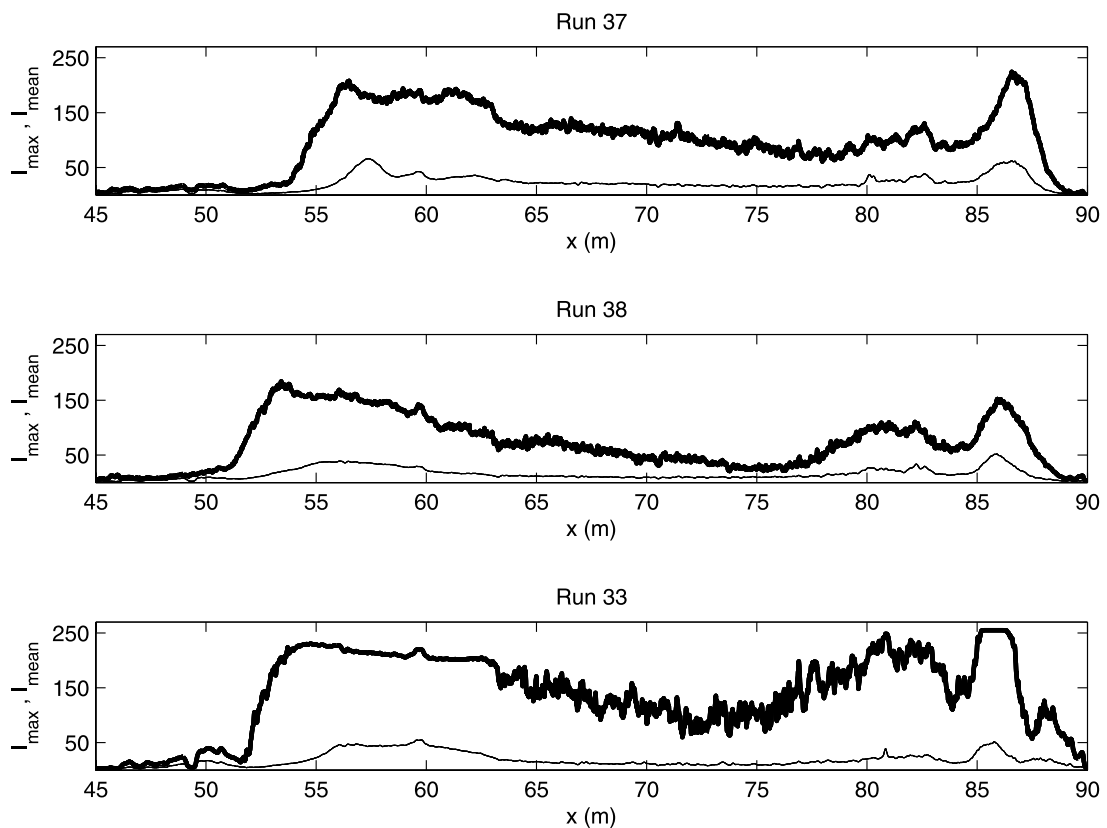**Figure 6.** (top) Phase-averaged time stack from run 36. (bottom) $I_{\max}$ (thick line) and I_{mean} (thin line).

Figure 7. $I_{\max}$ (thick line) and I_{mean} (thin line) for three experimental runs.
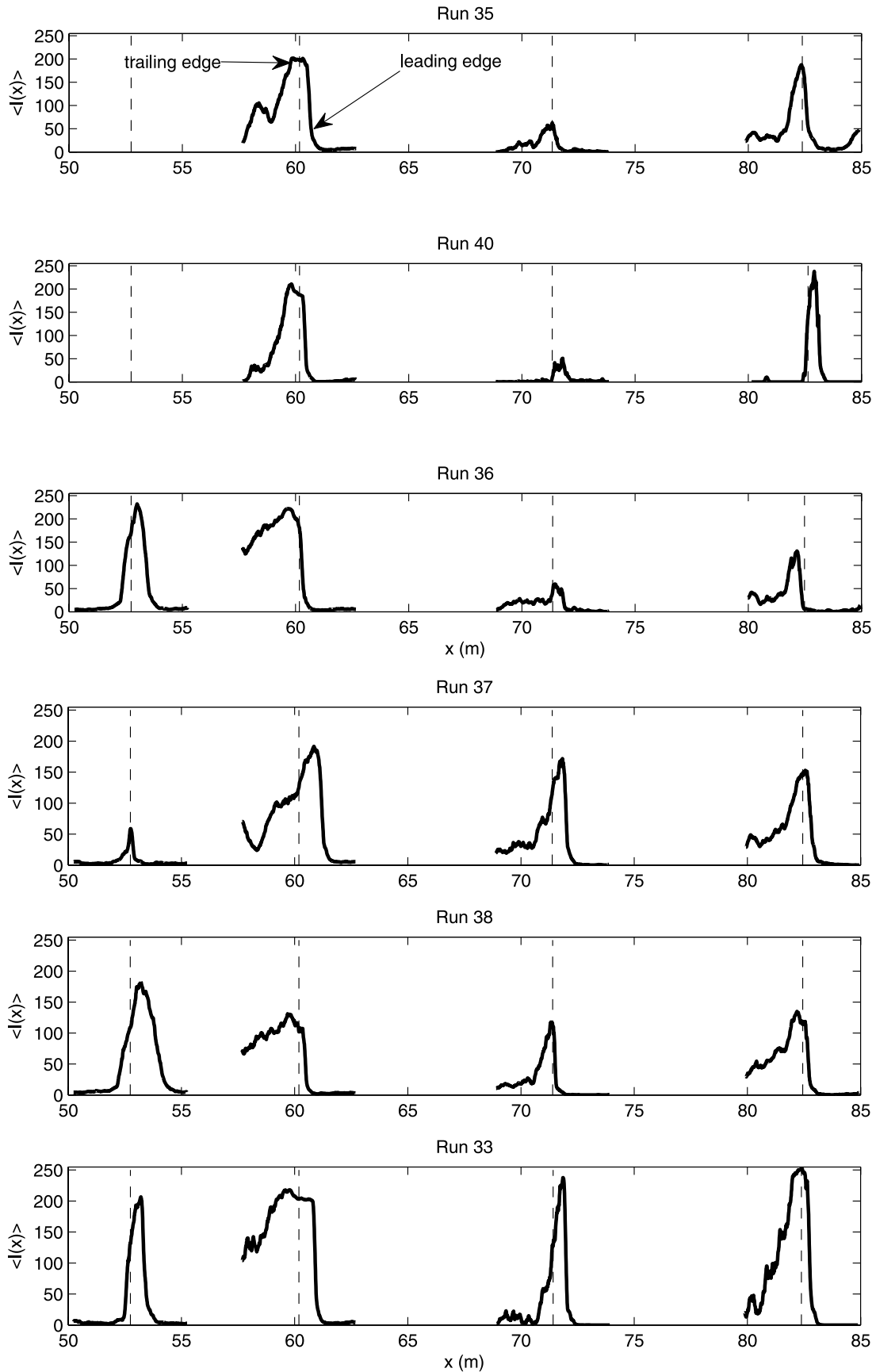
Figure 8. Spatial phase-averaged intensity signals at all wave gauge locations where significant breaking (>2%) occurred. Vertical dashed lines indicate wave gauge locations.
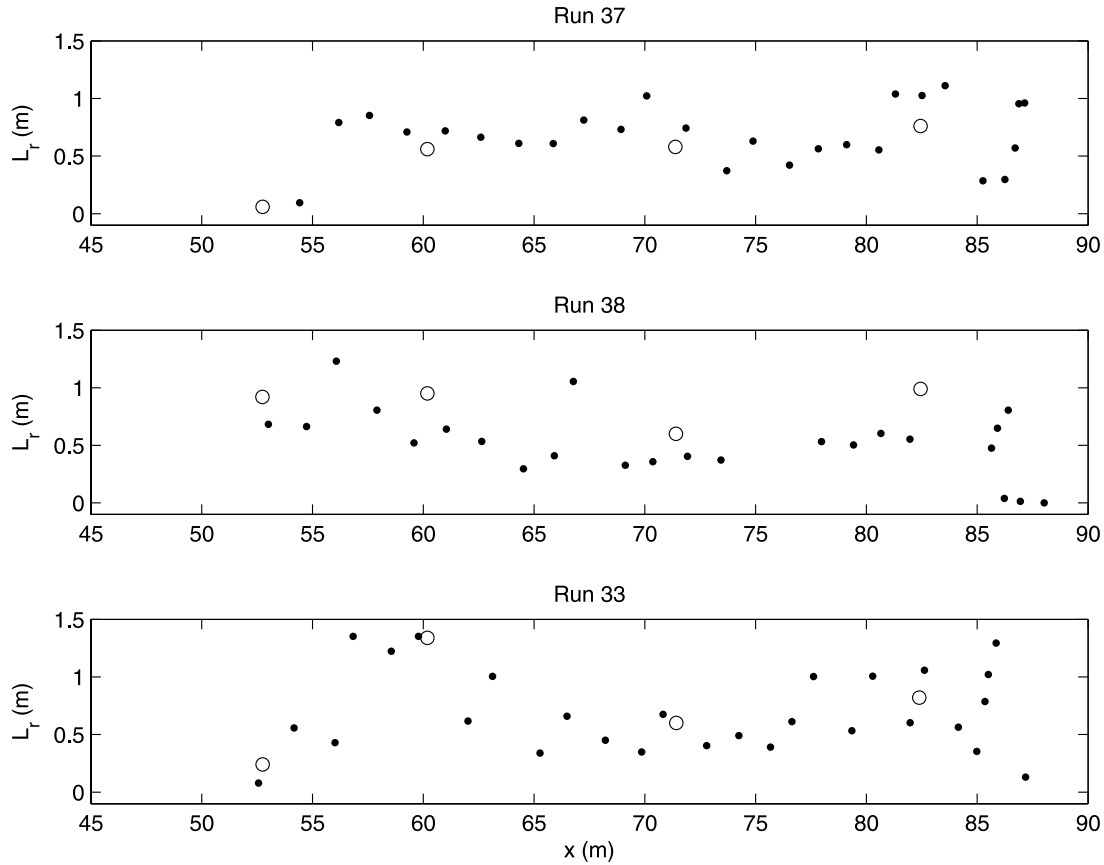
Figure 9. Length of the wave roller (L_r) in the cross-shore direction versus cross-shore location. Circles are determined from the spatial phase-averaged signal at the wave gauge locations, and dots are taken from phase-averaged time stacks.

individual wave may have a direct relationship to the amount of ongoing local dissipation as well. For the runs shown in Figure 8, wave breaking was more intense in the trough and there is little change in intensity magnitude as compared to over the bar.

5. Relationship Between Intensity Signal and Dissipation

5.1. Determination of Roller Length

[44] In this section we will ignore any variation of the local optical intensity at the wave crest as a wave propagates through the surf zone. Instead, we extract the physical size of the wave roller from the phase-averaged signal at different surf zone locations. As shown in section 2.2 roller lengths can be directly related to the local wave roller dissipation.

[45] On the basis of what we have learned from the results presented thus far, we define a method for extracting the cross-shore horizontal component of the length of the wave roller from the intensity data. At the leading edge of the roller (see Figure 8 (top plot)) we choose a threshold intensity value that is two standard deviations above the mean of the entire time stack, $I(x, t)$. The results are not sensitive to the exact value of this threshold and the front edge of the roller defined this way corresponds closely to the zero crossing of the water surface signal (see Figures 4

and 5). The trailing edge of the wave roller is defined as the point furthest offshore of the roller front that exhibits the maximum intensity, or in other words, as the point where the intensity begins to decrease in the offshore direction. The area between the roller front and trailing edge must be a continuous region of intensities above the threshold value.

[46] First concentrating on the three runs where the fraction of breaking waves was nearly 100% at gauges 2–5 (except gauge 2, run 37), we extracted the horizontal roller length, L_r, at each gauge location from the spatially phase-averaged data. The variation of the roller lengths through the surf zone is shown by the circles in Figure 9. These measurements were also corrected for the misregistration effect by adding the corrections given in Table 3 (Appendix A). The correction is only applied to the trailing edge location, since that has been shown to lie at the wave crest where misregistration is the largest. The location of the leading edge of the roller does not need correction as it lies very close to the vertical elevation of the still water level. The correction effectively shifts the trailing edge of the roller in the offshore direction (for gauges 3–6) and increases the roller length.

[47] The roller lengths in Figure 9 show the roller grows rapidly over the offshore bar ($x = 55$ m), decays somewhat through the trough region and then grows again at the shore break. We note that these roller lengths are rather different from what is assumed in the ad hoc model of

Table 3. Misregistration Corrections[a]

Run	WG 2 (m)	WG 3 (m)	WG 4 (m)	WG 5 (m)	WG 6 (m)
35	−0.19	0.01	0.14	0.35	0.41
40	−0.15	0.01	0.14	0.35	0.67
36	−0.23	0.01	0.13	0.37	0.51
37	−0.21	0.02	0.15	0.39	0.47
38	−0.23	0.01	0.15	0.41	0.47
33	−0.19	0.02	0.15	0.43	0.41

[a]Here x_g' is x_g plus correction. WG, wave gauge.

Aarninkhof and Ruessink [2004]. Their model assumes that the individual roller intensity signals have a duration of one-half the peak period, or that the roller length should be 50% of the local wavelength. This contrasts with the data of *Duncan* [1981], whose equilibrium roller lengths ranged from 21 to 40% of the local wavelength. In our observations the roller lengths are approximately 5–10% of the local wavelength calculated from linear wave theory.

[48] We consider the roller measurements that were made at the wave gauge locations on the basis of the spatial phase-averaged method using the passing wave crests identified in the wave gauge records to be the most accurate. However, we also attempted to fill in between the wave gauges by applying the roller measurement analysis to the phase-averaged time stack data (e.g., Figure 6). These data are also shown in Figure 9 (as dots) and indicate that while the data derived from the phase-averaged time stack are a bit noisier, they compare very well with the more rigorous measurements. Note that the agreement between the two measurements is not affected by the misregistration correction since the correction was applied to each; that is, the complete cross-shore variation of the correction was used for the time stack measurements.

5.2. Comparison to *Duncan*'s [1981] Measurements

[49] First, as a consistency check, we compare our roller measurements to those of *Duncan* [1981]. Those measurements were at a smaller scale and more precise (distances were accurate to ±0.2 cm). However, the experimental conditions were rather different. Since measurements of A were not feasible in our case, we instead measured the cross-shore roller length, L_r. This quantity is related to the along-slope length by $L_r = L_r' \cos \theta$. Figure 10 shows the cross-shore roller length versus local wave height from the *Duncan* [1981] data as well as from our observations using the spatial phase-averaged method. To ensure enough waves for the phase averaging, only data from locations where the fraction of breaking waves was large (greater than 36%) were used (see Table 2).

[50] In Figure 10, the scale difference between the two sets of measurements is immediately evident and a solid line representing the linear fit to *Duncan*'s [1981] data ($L_r = 2.91H$) is shown in order to facilitate comparison. The different symbols represent different cross-shore locations and thus different stages of the roller life cycle. We can see from Figure 10 that the ratios (L_r/H) from gauges 3 and 5 compare very well with the previous data, while the other two gauges show relatively shorter roller lengths in comparison. The nonconstant nature of this ratio through the surf zone is similar to that found by *Govender et al.* [2002] for the related ratio of A/H^2. *Dally and Brown* [1995] also pointed out that a constant A/H^2 ratio is unrealistic during

the growth phase of the roller. The fact that the roller length (or A) is not always simply correlated with H (or H^2) can be understood by noting that the measurements of *Duncan* [1981] are from wave rollers in equilibrium. On the other hand, in the surf zone the wave roller must go through at least one growth and decay cycle, and perhaps multiple cycles if more than one sandbar is present.

[51] As described in section 4.1, at gauges 3 and 5 the roller was well established, i.e., close to an equilibrium condition where we might expect the L_r/H ratio to be similar to that of *Duncan*'s [1981] data. Gauge 2 was located near the plunge point and the ratio there shows the biggest differences from the equilibrium results. The roller was generally decaying through the trough of the bar (gauge 4) and there the ratio would be expected to be smaller because the roller lengths decrease as the roller decays in strength and the wave heights recover. Overall, this comparison gives us good confidence in our roller measurements.

5.3. Model/Data Comparisons

[52] The previous comparisons have demonstrated that it is possible to extract physically realistic roller length measurements from the intensity observations, next we test whether these measurements can be used to determine wave roller dissipation through equation (1) by comparing the measurements with predictions from a model for wave roller transformation in the surf zone.

[53] As mentioned previously, our approach here is different from previous approaches in that we use the optical signal to measure a physical quantity, the roller length, that is directly related to both roller energy and roller dissipation. The roller dissipation through the surf zone can be modeled with two coupled differential equations. The first describes the transformation of organized wave energy in the cross-shore direction:

$$\frac{\partial}{\partial x}\left(E_w C_g\right) = -D_w, \qquad (3)$$

where $E_w = \frac{1}{8}\rho g H^2$ is the average organized wave energy, C_g is the group velocity, and D_w is the breaking-induced dissipation. Several models for the dissipation term in equation (3) have been given in the literature [e.g., *Battjes and Janssen*, 1978; *Thornton and Guza*, 1983; *Baldock et*
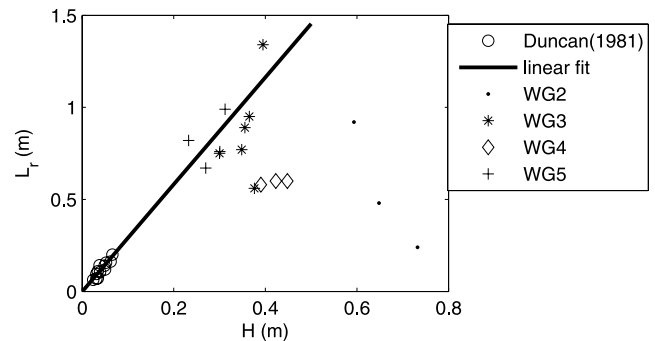

Figure 10. Cross-shore component of observed roller lengths versus local breaking wave height. Circles are data reproduced from *Duncan* [1981].
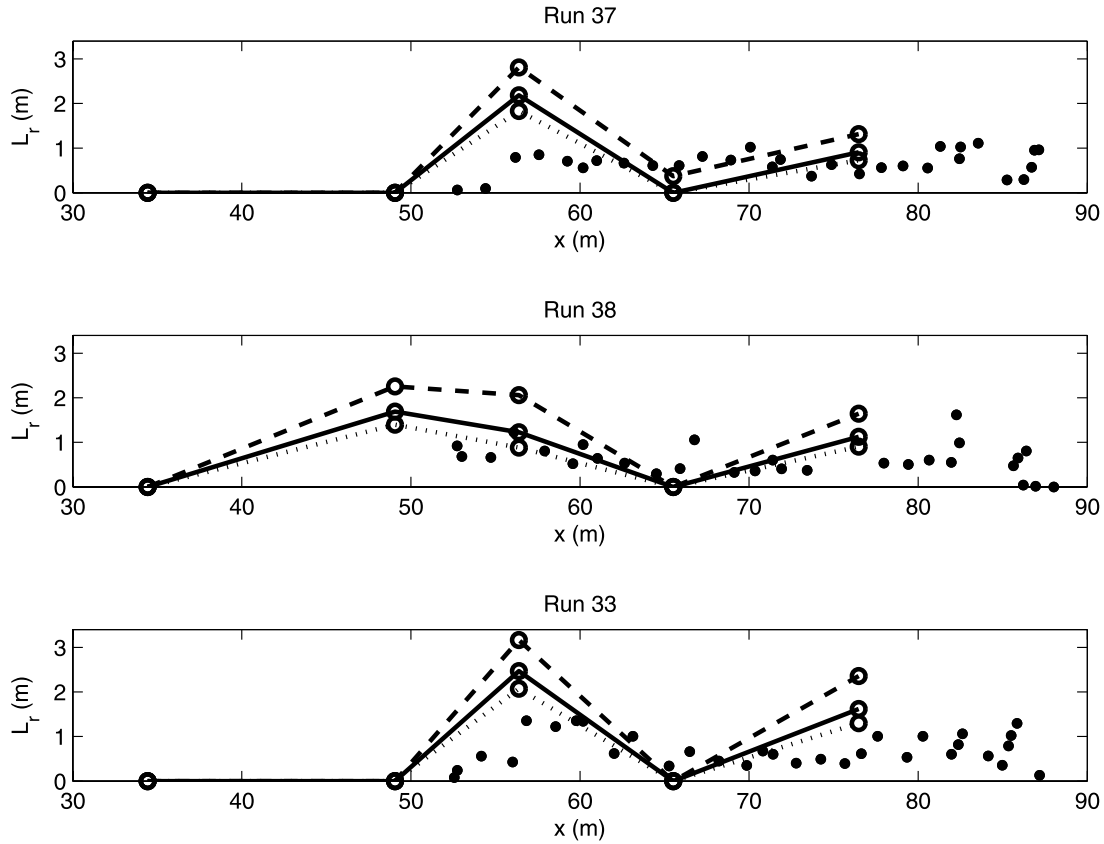
Figure 11. Roller lengths versus cross-shore distance for (top) run 37, (middle) run 38, and (bottom) run 33. Optical measurements are shown as solid circles, and open circles with lines are model outputs with $\theta = 5.0°$ (dashed), $\theta = 12.6°$ (solid), and $\theta = 20.0°$ (dotted).

al., 1998]. Alternately, if wave and bathymetry measurements are available, then the term on the left-hand side can be treated as known and we can calculate D_w directly.

[54] In the surf zone the breaking-induced dissipation term serves as a source term in the energy balance for the roller given by [Nairn et al., 1990; Stive and de Vriend, 1994]

$$\frac{\partial}{\partial x}(E_r C) = -D - \frac{\partial}{\partial x}(E_w C_g), \qquad (4)$$

where the roller dissipation D was defined in equation (1) and the roller energy is defined as [Svendsen, 1984]

$$E_r = \frac{\rho A C}{2T}. \qquad (5)$$

[55] Next, considering ρ, g, C, θ, and T as known parameters, we rewrite equation (4) as a forward model for the roller cross-sectional area:

$$\frac{d}{dx}\left(\rho C^2 \frac{A}{2T}\right) + \rho g \frac{A}{T} \sin\theta\cos\theta = -\frac{d}{dx}(E_w C_g), \qquad (6)$$

where the right-hand side can be calculated directly from wave height and bathymetry measurements and using the

linear dispersion relation. The equation is solved using a central difference scheme in space about the midpoints between wave measurements, which follows closely the method of Dally and Brown [1995]. Here, we convert the modeled roller areas to roller lengths using $L_r = \cos\theta\sqrt{A/0.11}$ (equation (2)) and the model predictions are compared with observations in Figure 11.

[56] Equation (6) depends explicitly on the wave slope θ, which is often taken as a calibration parameter in wave roller transformation models and treated as a time-independent and cross-shore uniform constant [Ruessink et al., 2001]. Some example values given in the literature are ~6° [Dally and Brown, 1995; Reniers and Battjes, 1997] and 2.9° [Ruessink et al., 2001]. Duncan [1981] reported a range of $10.0° \leq \theta \leq -14.7°$ with a mean of 12.6°. However, generally speaking the wave slope will vary in both space and time. In Figure 11 we have used three different constant slope values, $\theta = 5°$, $\theta = 12.6°$, and $\theta = 20°$. Figure 11 shows that the observed roller lengths exhibit a similar magnitude and cross-shore variation as that predicted by the model driven by the observed wave height transformation. The model predicted roller lengths near the onset of breaking over the bar are somewhat larger than observed and the reason for this will become more clear in section 6. The predicted lengths also show some dependence on wave slope with the best agreement when $\theta = 20°$, but they are not considerably better than when $\theta = 12.6°$.

Overall, these results confirm that the observed roller lengths can be directly related to the local dissipation.

6. Discussion of Potential Inverse Model

[57] In the field, surf zone wave heights can only be measured by in situ instruments, which are difficult to maintain because of the high wave energies that often occur. Hence, it is of interest to examine another potential use for remote sensing measurements of wave roller transformation, that of estimating wave heights through an inverse solution to equation (6). In this approach, we obtain the cross-shore variation of wave height by solving for $E_w Cg$ using a forward difference scheme in space given by

$$(E_w Cg)_{i+1} = (E_w Cg)_i + \frac{\rho}{2T}\left[(C^2 A)_i - (C^2 A)_{i+1} \right] - \frac{\Delta x \rho g}{T}(A \sin\theta \cos\theta)_i, \qquad (7)$$

where A is calculated from the roller observations using

$$A = 0.11\left(\frac{L_r}{\cos\theta}\right)^2. \qquad (8)$$

The calculation is initialized with the incident wave energy flux measured at the furthest offshore gauge. Since the roller lengths are highly resolved in space, we perform this calculation on a uniform $\Delta x = 0.01$ m grid and a simpler forward difference scheme is sufficient. All of the roller length observations shown in Figure 9 were fit with a smoothed cubic spline and interpolated to the finite difference grid and then used as input for the calculation. The splines of the roller lengths are shown in Figures 12b, 12d, and 13 (bottom).

[58] Once again, the wave slope needs to be specified for this calculation. Two of the curves shown in Figures 12a, 12c, and 13 (top) correspond to the wave heights calculated using cross-shore constant values of $\theta = 12.6°$ and $\theta = 20.0°$. As would be expected from the results of section 5.3, the wave heights from the inverse model using $\theta = 20°$ show the best agreement with the measured values.

[59] In addition, we can see from these calculations why the forward model-predicted roller lengths over the bar were larger than the observations. Essentially, that resulted from the failure of linear wave theory near the break point. This can be seen by the fact that the observed roller lengths leading up to the break point are essentially zero, which means that $A = 0$ in equation (7) in this region and the inverse model reduces to the simple conservation of wave energy flux. Hence, the underestimate of the inverse-modeled wave heights at the break point seen in Figures 12 and 13 has nothing to do with the roller observations, which we have confirmed by artificially setting $A = 0$ in the shoaling zone, negating any effect of the cubic spline. Instead, it is instead the likely result of nonlinear shoaling effects. These effects are known to be significant for nonlinear regular waves in particular [see *Tsai et al.*, 2001; *Tajima and Madsen*, 2006].

[60] The underestimate of wave shoaling to the break point by linear theory translates into an overestimate of roller size in the region just after the break point (over the bar) because the model-predicted roller size (equation (6) and Figure 11) is driven by the steep wave energy flux gradient there, which is inconsistently large. Restated, at the break point the quantity $E_w Cg$ is overestimated using linear theory and the wave measurements and this translates into an overestimate of the roller size. An alternative explanation for the failure in linear shoaling is the occurrence of reflections from the bar, which would increase the wave heights measured over the bar because of the presence of a partial standing wave. This process would have the same effect on the modeled roller sizes and inverse-modeled wave heights.

[61] While there are significant differences between the inverse-modeled wave heights and the measurements, it would be arguably more fair to judge the inverse model on its ability to capture the integrated decay through the surf zone, i.e., by comparing the wave heights at the most shoreward wave gauge. Good agreement at this location indicates that the roller observations reasonable capture the total decay of energy flux incident from offshore where the calculated $E_w Cg$ should be reasonably accurate.

[62] Finally, we find it of interest to note that the presence of roller observations removes the need for specifying a constant wave slope, which then allows for more accurate estimates of the roller dissipation and improves the wave height predictions from the inverse model. Specifically, *Duncan*'s [1981] results also showed that

$$H_b = 1.6 L_r' \sin\theta \quad \text{or} \quad \theta = \tan^{-1}\left(\frac{H_b}{1.6 L_r}\right). \qquad (9)$$

Therefore, θ can be calculated locally from the local roller length using the breaking wave height from the previous spatial step. Including this cross-shore variable θ makes some improvement in the wave heights from the inverse model as shown in Figures 12 and 13. For comparison, the slopes determined in this way at the cross-shore locations of the three shoreward wave gauges are 19.5°, 24.2°, and 16.3°.

7. Conclusions

[63] We have presented an analysis of the optical intensity signals from individual, nearshore breaking waves. The laboratory surf zone consisted of a fixed bed bar/trough morphology and the optical remote sensing observations capture the growth, equilibrium, and decay phases of the wave breaking roller. The analysis utilized several different phase-averaging methodologies and the phase-averaged intensity signals were compared with the underlying water surface variations measured by in situ wave gauges. The optical intensities were shown to sharply increase from toe of the wave roller with the maxima located at the wave crests. In comparison to the traditional time exposure, the local maxima of the phase-averaged signals were also shown to better describe the location of the onset of wave breaking and to more clearly indicate the occurrence of wave breaking in the trough.

[64] Next, the phase-averaged signals were used to determine the cross-shore length of the wave roller throughout the surf zone and the measured roller lengths were tested for consistency against the smaller-scale observations of
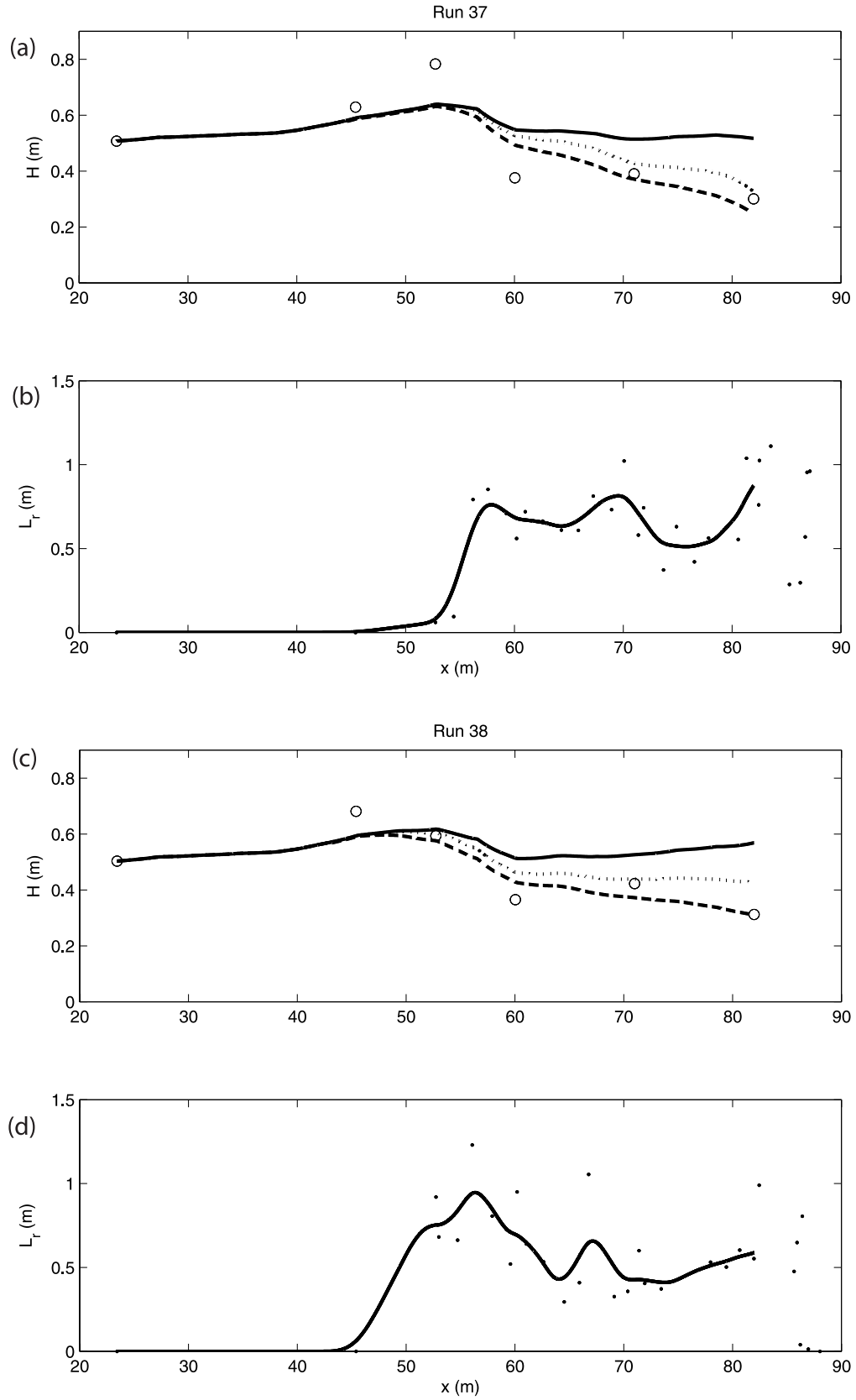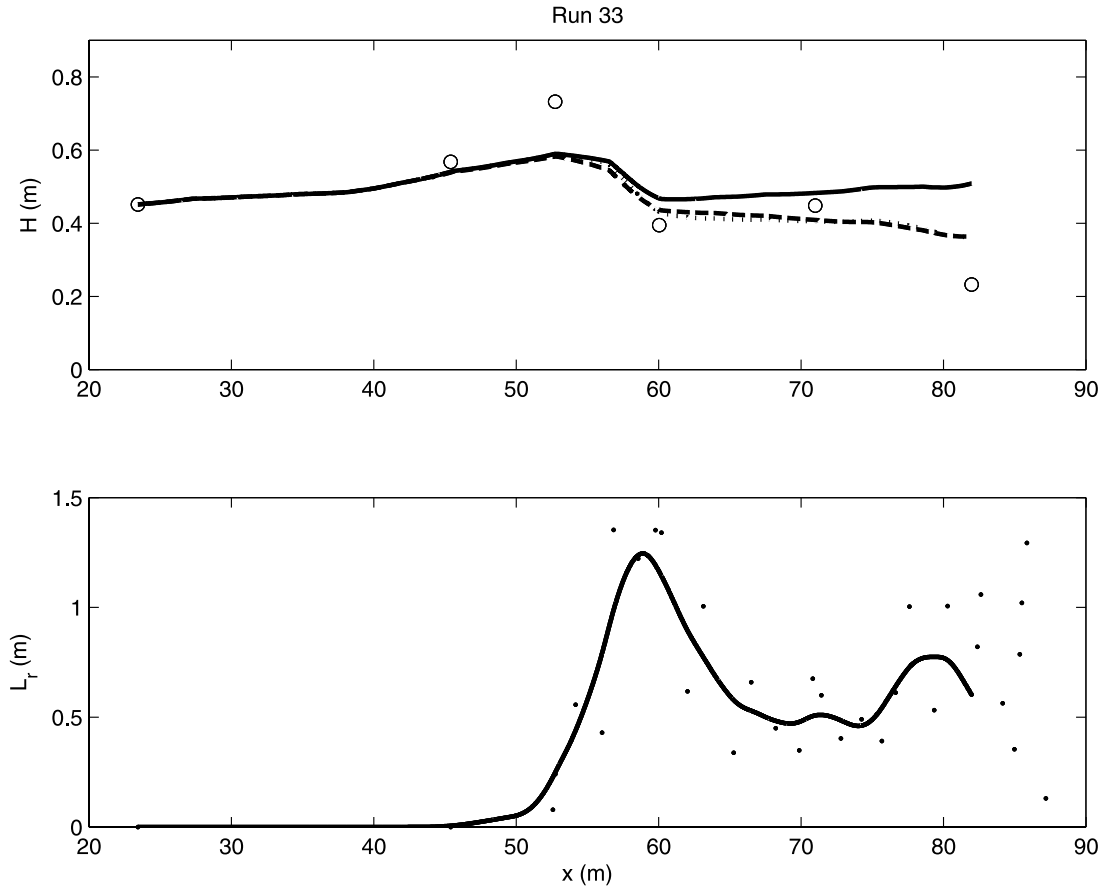
Figure 12. (a) Measured wave heights for run 37 (circles) and inverse modeled wave heights shown as lines: $\theta = 12.6°$ (solid), $\theta = 20.0°$ (dotted), and θ from equation (9) (dashed). (b) Observed roller lengths shown as dots and spline fit shown as solid line. (c) Measured wave heights for run 38 (circles) and inverse modeled wave heights shown as lines: $\theta = 12.6°$ (solid), $\theta = 20.0°$ (dotted), and θ from equation (9) (dashed). (d) Observed roller lengths shown as dots and spline fit shown as solid line.

Figure 13. (top) Measured wave heights for run 33 (circles) and inverse modeled wave heights shown as lines: $\theta = 12.6°$ (solid), $\theta = 20.0°$ (dotted), and θ from equation (9) (dashed). (bottom) Observed roller lengths shown as dots and spline fit shown as solid line.

Duncan [1981]. At locations in the surf zone where the roller would be expected to be in near-equilibrium conditions, the measured roller lengths showed the same variation with breaking wave heights as was found in the previous work. The observed roller lengths were also shown to compare well with predictions from a standard wave roller transformation model for the tested wave conditions. These results demonstrate that observations of roller lengths can be used as a more physical link between the remotely sensed signal and surf zone wave dissipation. This link may enable the use of observations of the space/time variation of wave breaking, at the scales of individual waves, to be used to analyze the variable forcing of surf zone currents.

[65] Finally, a simple inverse model was developed to test whether observed roller lengths could be used to estimate wave height transformation through the surf zone. Initial results using a limited set of wave conditions were encouraging. Future work will involve testing all of the above results under random wave conditions and at field scales.

Appendix A: Experimental Procedures

A1. Time Synchronization

[66] Time synchronization of the cameras and wave gauges was achieved using a novel combination of an in situ wave gauge ($x = 23.45$ m) and a remote optical wave gauge. The latter consisted of a vertical pixel array projected onto the flume wall opposite to the cameras and at the same cross-shore location. The contrast between the unbroken water surface and the wall allowed optical tracking of the water/wall interface. Cross-spectral analysis of the in situ and optical gauge time series showed high levels of coherence (typically $\gamma^2 > 0.75$ at frequencies up to 0.7 Hz). Visual inspection of the occurrence of the first wave packet was used to determine the time offset between the sensor clocks, thus allowing synchronization. We estimate that synchronization between the in situ gauges and the cameras was achieved to within ±1 frame (±0.1 s).

A2. Misregistration Correction

[67] The corrected crest locations in the pixel array, x'_g, differ from the actual gauge locations, x_g, because of the finite amplitude of the wave crests. This is a local correction for projection error and is dependent on the vertical elevation of the wave crest above the datum used for image registration and on the camera viewing geometry. The value of the correction increases for larger wave heights and smaller camera grazing angles (i.e., distance from the cameras). Table 3 gives the correction values for each wave gauge and wave condition. Details of this calculation can be found in the work by *Catalán* [2005].

References

Aarninkhof, S. G. J., and B. G. Ruessink (2004), Video observations and model predictions of depth-induced dissipation, *IEEE Trans. Geosci. Remote Sens.*, 42(11), 2612–2622, doi:10.1109/TGRS.2004.835349.

Aarninkhof, S. G. J., B. G. Ruessink, and J. A. Roelvink (2005), Nearshore subtidal bathymetry from time-exposure video images, *J. Geophys. Res.*, 110, C06011, doi:10.1029/2004JC002791.

Baldock, T. E., P. Holmes, S. Bunker, and P. V. Weert (1998), Cross-shore hydrodynamics within an unsaturated surf zone, *Coastal Eng.*, 34, 173–196, doi:10.1016/S0378-3839(98)00017-9.

Battjes, J. A., and J. P. F. Janssen (1978), Energy loss and set-up due to breaking of random waves, in *Proceedings of Sixteenth Coastal Engineering Conference*, pp. 569–587, Am. Soc. of Civ. Eng., New York.

Bondur, V., and E. Sharkov (1982), Statistical properties of whitecaps on a rough sea, *Oceanology*, Engl. Transl., 22, 274–279.

Callaghan, A. H., G. B. Deane, and M. D. Stokes (2008), Observed physical and environmental causes of scatter in whitecap coverage values in a fetch-limited coastal zone, *J. Geophys. Res.*, 113, C05022, doi:10.1029/2007JC004453.

Catalán, P. A. (2005), Hybrid approach to estimating bathymetry using remote sensing, M.Oc.E. thesis, Oreg. State Univ., Corvallis.

Catalán, P., and M. Haller (2008), Remote sensing of breaking wave phase speeds with application to nonlinear depth inversion, *Coastal Eng.*, 55, 93–111, doi:10.1016/j.coastaleng.2007.09.010.

Catalán, P. A., M. C. Haller, R. A. Holman, and W. J. Plant (2008), Surf zone breaking wave identification using marine radar, in *Coastal Engineering 2008: Proceedings of the Thirty-First International Conference*, vol. 1, edited by J. McKee Smith, pp. 60–72, Am. Soc. of Civ. Eng., New York.

Dally, W. R., and C. A. Brown (1995), A modeling investigation of the breaking wave roller with application to cross-shore currents, *J. Geophys. Res.*, 100(C12), 24,873–24,883, doi:10.1029/95JC02868.

Duncan, J. (1981), An experimental investigation of breaking waves produced by a towed hydrofoil, *Proc. R. Soc. London, Ser. A*, 377(1770), 331–348.

Gordon, H. R., and M. M. Jacobs (1977), Albedo of the ocean-atmosphere system: Influence of sea foam, *Appl. Opt.*, 16(8), 2257–2260.

Govender, K., G. P. Mocke, and M. J. Alport (2002), Video-imaged surf zone wave and roller structures and flow fields, *J. Geophys. Res.*, 107(C7), 3072, doi:10.1029/2000JC000755.

Haller, M. C., and D. R. Lyzenga (2003), Comparison of radar and video observations of shallow water breaking waves, *IEEE Trans. Geosci. Remote Sens.*, 41(4), 832–844, doi:10.1109/TGRS.2003.810695.

Haller, M. C., and H. T. Özkan Haller (2007), Waves on unsteady currents, *Phys. Fluids*, 19(12), 126601, doi:10.1063/1.2803349.

Holman, R., and J. Stanley (2007), The history and technical capabilities of Argus, *Coastal Eng.*, 54, 477–491, doi:10.1016/j.coastaleng.2007.01.003.

Jessup, A. T., C. J. Zappa, M. R. Loewen, and V. Hesany (1997), Infrared remote sensing of breaking waves, *Nature*, 385, 52–55, doi:10.1038/385052a0.

Kerman, B. R., and L. Dernier (1994), Multifractal representation of breaking waves on the ocean surface, *J. Geophys. Res.*, 99(C8), 16,179–16,196.

Kraan, G., W. Oost, and P. Janssen (1996), Wave energy dissipation by whitecaps, *J. Atmos. Oceanic Technol.*, 13(1), 262–267, doi:10.1175/1520-0426(1996)013<0262:WEDBW>2.0.CO;2.

Lafon, C., J. Piazzola, P. Forget, O. Le Calve, and S. Despiau (2004), Analysis of the variations of the whitecap fraction as measured in a coastal zone, *Boundary Layer Meteorol.*, 111(2), 339–360, doi:10.1023/B:BOUN.0000016490.83880.63.

Lippmann, T. C., and R. A. Holman (1989), Quantification of sandbar morphology: A video technique based on wave dissipation, *J. Geophys. Res.*, 94(C1), 995–1011.

Lippmann, T. C., and R. A. Holman (1991), Phase speed and angle of breaking waves measured with video techniques, in *Coastal Sediments '91*, vol. 1, edited by N. C. Kraus, K. J. Gingerich, and D. L. Kriebel, pp. 542–556, Am. Soc. of Civ. Eng., New York.

Marmorino, G. O., and G. B. Smith (2005), Bright and dark ocean whitecaps observed in the infrared, *Geophys. Res. Lett.*, 32, L11604, doi:10.1029/2005GL023176.

McGregor, J. A., E. M. Poulter, and M. J. Smith (1998), S band Doppler radar measurements of bathymetry, wave energy fluxes, and dissipation across an offshore bar, *J. Geophys. Res.*, 103(C9), 18,779–18,789.

McNinch, J. E. (2007), Bar and Swash Imaging Radar (BASIR): A mobile X-band radar designed for mapping nearshore sand bars and swash-defined shorelines over large distances, *J. Coastal Res.*, 23(1), 59–74, doi:10.2112/05-0452.1.

Melville, W. K., and R. J. Rapp (1985), Momentum flux in breaking waves, *Nature*, 317, 514–516, doi:10.1038/317514a0.

Monahan, E. C., and D. K. Woolf (1989), Comments on "Variations of whitecap coverage with wind stress and water temperature," *J. Phys. Oceanogr.*, 19(5), 706–709, doi:10.1175/1520-0485(1989)019<0706:COOWCW>2.0.CO;2.

Nairn, R. B., J. A. Roelvink, and H. N. Southgate (1990), Transition zone width and implications for modeling surfzone hydrodynamics, in *Proceedings of the Twenty-Second Coastal Engineering International Conference*, edited by B. L. Edge, pp. 68–81, Am. Soc. of Civ. Eng., New York.

Reniers, A., and J. Battjes (1997), A laboratory study of longshore currents over barred and non-barred beaches, *Coastal Eng.*, 30, 1–22, doi:10.1016/S0378-3839(96)00033-6.

Ross, D. B., and V. Cardone (1974), Observations of oceanic whitecaps and their relation to remote measurements of surface wind speed, *J. Geophys. Res.*, 79(3), 444–452.

Ruessink, B. G., J. R. Miles, F. Feddersen, R. T. Guza, and S. Elgar (2001), Modeling the alongshore current on barred beaches, *J. Geophys. Res.*, 106(C10), 22,451–22,463, doi:10.1029/2000JC000766.

Ruessink, B. G., P. S. Bell, I. M. J. van Enckevort, and S. G. J. Aarninkhof (2002), Nearshore bar crest location quantified from time-averaged X-band radar images, *Coastal Eng.*, 45, 19–32, doi:10.1016/S0378-3839(01)00042-4.

Stilwell, D. (1969), Directional energy spectra of the sea from photographs, *J. Geophys. Res.*, 74(8), 1974–1986.

Stive, M. J. F., and H. J. de Vriend (1994), Shear stresses and mean flow in shoaling and breaking waves, in *Coastal Engineering 1990: Proceedings of the Twenty-Fourth International Conference*, edited by B. L. Edge, pp. 594–608, Am. Soc. of Civ. Eng., New York.

Stramska, M., and T. Petelski (2003), Observations of oceanic whitecaps in the north polar waters of the Atlantic, *J. Geophys. Res.*, 108(C3), 3086, doi:10.1029/2002JC001321.

Sugihara, Y., H. Tsumori, T. Ohga, H. Yoshioka, and S. Serizawa (2007), Variation of whitecap coverage with wave-field conditions, *J. Mar. Syst.*, 66(1–4), 47–60, doi:10.1016/j.jmarsys.2006.01.014.

Svendsen, I. A. (1984), Wave heights and set-up in a surf zone, *Coastal Eng.*, 8, 303–329, doi:10.1016/0378-3839(84)90028-0.

Svendsen, I. A. (2006), *Introduction to Nearshore Hydrodynamics*, Adv. Ser. Ocean Eng., vol. 24, World Sci., River Edge, N. J.

Tajima, Y., and O. S. Madsen (2006), Modeling near-shore waves, surface rollers, and undertow velocity profiles, *J. Waterw. Port Coastal Ocean Eng.*, 132(6), 429–438, doi:10.1061/(ASCE)0733-950X(2006)132:6(429).

Thornton, E. B., and R. T. Guza (1983), Transformation of wave height distribution, *J. Geophys. Res.*, 88(C10), 5925–5938.

Tratt, D. M., R. T. Menzies, M. P. Chiao, D. R. Cutten, J. Rothermel, R. M. Hardesty, J. N. Howell, and S. L. Durden (2002), Airborne Doppler lidar investigation of the wind-modulated sea-surface angular retroreflectance signature, *Appl. Opt.*, 41(33), 6941–6949.

Tsai, C.-P., H.-B. Chena, and J. R. C. Hsu (2001), Calculations of wave transformation across the surf zone, *Ocean Eng.*, 28(8), 941–955, doi:10.1016/S0029-8018(00)00047-0.

van Dongeren, A., N. Plant, A. Cohen, D. Roelvink, M. C. Haller, and P. Catalán (2008), Beach Wizard: Nearshore bathymetry estimation through assimilation of model computations and remote observations, *Coastal Eng.*, 55, 1016–1027, doi:10.1016/j.coastaleng.2008.04.011.

van Enckevort, I. M. J., and B. G. Ruessink (2001), Effect of hydrodynamics and bathymetry on video estimates of nearshore sandbar position, *J. Geophys. Res.*, 106(C8), 16,969–16,979, doi:10.1029/1999JC000167.

Walker, R. E. (1994), *Marine Light Field Statistics*, John Wiley, New York.

————————

P. A. Catalán, Departamento de Obras Civiles, Universidad Técnica Federico Santa María, Casilla 110-V, Valparaiso, Chile.

M. C. Haller, Coastal and Ocean Engineering Program, School of Civil and Construction Engineering, Oregon State University, 220 Owen Hall, Corvallis, OR 97331, USA. (hallerm@engr.orst.edu)